Coupled Large Amplitude Motions: The Effects of Two Methyl Internal Rotations and 14 N Quadrupole Coupling in 4,5-Dimethylthiazole Investigated by Microwave Spectroscopy

Vinh Van, Thuy Nguyen, Wolfgang Stahl, Ha Vinh Lam Nguyen, Isabelle Kleiner

Coupled Large Amplitude Motions: The Effects of Two Methyl Internal Rotations and ^{14}N Quadrupole Coupling in 4,5-Dimethylthiazole Investigated by Microwave Spectroscopy

Vinh Van,[a] Thuy Nguyen,[b] Wolfgang Stahl,[a] Ha Vinh Lam Nguyen,[b] and Isabelle Kleiner[b**]*

[a] Institute of Physical Chemistry, RWTH Aachen University, Landoltweg 2, D-52074 Aachen, Germany

[b] Laboratoire Interuniversitaire des Systèmes Atmosphériques (LISA), CNRS UMR 7583, Université Paris-Est Créteil, Université de Paris, Institut Pierre Simon Laplace (IPSL), 61 avenue du Général de Gaulle, F-94010 Créteil cedex, France.

*Corresponding author: Email: lam.nguyen@lisa.u-pec.fr

** This paper is dedicated to Dr. Jon T. Hougen, who was the mentor of our careers and our friend for so many years. Without his careful work, checking, and his love for spectroscopy, the present research would not be conducted in this form.

Abstract

The molecular jet Fourier-transform microwave spectrum of 4,5-dimethylthiazole has been recorded between 2.0 and 26.5 GHz, revealing torsional splittings arising from two inequivalent methyl internal rotations with relatively low hindering barriers and nitrogen quadrupole hyperfine structures. Two global fits with 1009 hyperfine components of 315 rotational transitions involving five torsional species were performed using the program *XIAM* and *BELGI-C_s-2Tops-hyperfine*, an extended version of the *BELGI-C_s-2Tops* code which includes the effect of the ^{14}N quadrupole coupling, giving a root-mean-square deviation of 399.8 kHz and 4.2 kHz, respectively. Compared to the monomethyl substituted thiazole derivatives, the barriers to internal rotation are drastically lower. This is also in contrast to chemical intuition which suggests high barriers due to steric hindrance. Because of the strong interaction between the methyl groups, strong top-top couplings in both the potential energy and kinetic parts of the Hamiltonian were observed.

Keywords: internal rotation, large amplitude motions, quadrupole hyperfine structure, rotational spectroscopy, dimethylthiazole

1. Introduction

Thiazole is a five-membered heterocyclic compound that contains a sulfur atom and a nitrogen atom in the ring. It exists as the basic structure element in a variety of organic compounds such as vitamin B_1 and clomethiazole [1]. It is also a precursor in the production of fungicides, drugs (e.g. alagebrium), and dyes [2]. Thiazole derivatives participate in several biosyntheses as required for the formation of thiamine [1], where the sulfur atom is obtained from cysteine. Whereas thiazoles are well-represented in biomolecules, their related compounds oxazoles, where the sulfur atom is replaced by an oxygen atom, are not.

Thiazole and its monomethyl derivatives have been studied thoroughly by microwave spectroscopy (see Figure 1) [3-6]. Whereas their structures are proved to be relatively rigid, the internal dynamics arising from the internal rotation of the substituted methyl group are hard to predict. It is particularly interesting to compare the hindering potentials of the methyl rotors, which strongly depend on the position of the methyl substituent. While changing the methyl group from the 4- (**3**) [5] to the 5-position (**4**) [6] does not significantly influence the hindering potential (357.6 cm^{-1} and 332.0 cm^{-1}, respectively), it decreases drastically to one tenth in 2-methylthiazole (**2**, 34.9 cm^{-1}, for molecule numbering see Figure 1) [4]. The same trend can be recognized in the related compounds, oxazoles, where the hindering potentials are 251.8 cm^{-1}, 428.0 cm^{-1}, and 477.9 cm^{-1} for 2- (**6**) [7], 4- (**7**) [8], and 5-methyloxazole (**8**) [7], respectively. It is also notable by comparing (**2**) and (**6**), (**3**) and (**7**), as well as (**4**) and (**8**) that substitution of an oxygen by a sulfur atom significantly reduces the hindering potential. An explanation for these observations is the aromatic character of azole rings. Thiazoles are characterized by larger π-electron delocalization than the corresponding oxazoles and have therefore greater aromaticity. This aromaticity is evidenced by the chemical shift of the ring protons in ^{1}H-NMR spectroscopy, which is between 7.27 and 8.77 ppm. It clearly indicates a strong diamagnetic ring current. The calculated π-electron density marks the 5-position as the primary site for electrophilic substitution and the 2-position as the site for nucleophilic substitution [9].

The question of how the hindering potentials are influenced if two positions in the thiazole ring are substituted by methyl groups prompted us to study 4,5-dimethylthiazole (**5**) (45DMTA). To the best of our knowledge, only two dimethyl substituted aromatic five-membered heterocyclic compounds, 2,5-dimethylthiophene [10] and 2,5-dimethylfuran [11], have been studied by microwave spectroscopy so far.

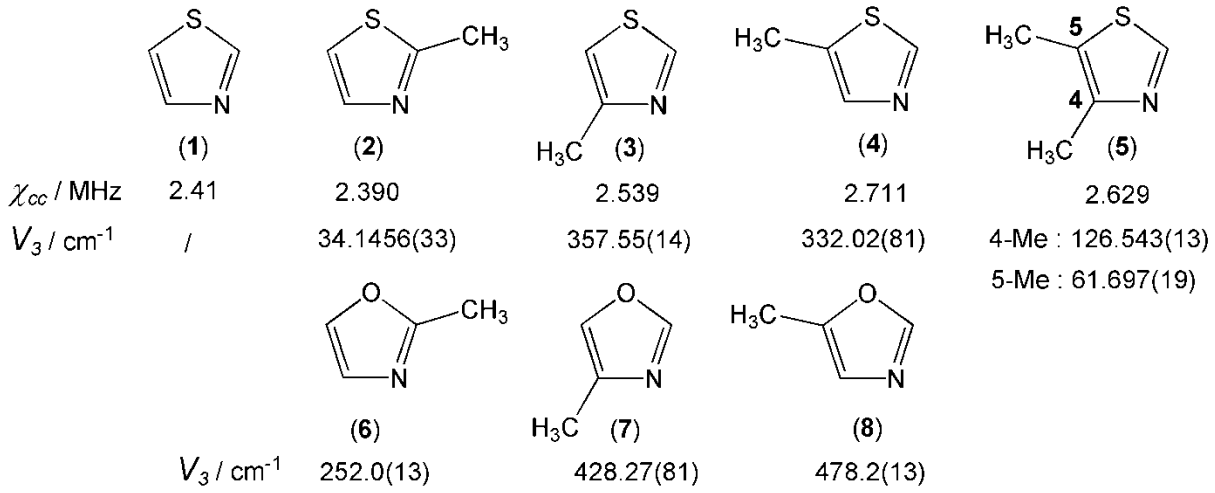

Figure 1: The ^{14}N quadrupole coupling constant χ_{cc} (in MHz) of thiazole and its methyl-substituted derivatives as well as methyl torsional barriers in methyl substituted thiazoles and oxazoles (in cm^{-1}). (**1**) Thiazole, (**2**) 2-methylthiazole [4], (**3**) 4-methylthiazole [5], (**4**) 5-methylthiazole [6], (**5**) 4,5-dimethylthiazole (this work), (**6**) 2-methyloxazole [7], (**7**) 4-methyloxazole [8], (**8**) 5-methyloxazole [7].

Because 45DMTA has in addition to the two methyl tops a ^{14}N nucleus with a nuclear spin $I = 1$, hyperfine splittings occur in the microwave spectrum. Currently, the combination of two methyl internal rotations with one ^{14}N quadrupole coupling can be treated with only one program, the *XIAM* code, where nuclear quadrupole interactions are treated in a first order approximation [12]. However, spectra of molecules with low barriers to internal rotation often cannot be modeled correctly with *XIAM* due to the limited number of fit parameters [13-15]. Implementing higher order terms in the program is a difficult task.

The disadvantages of the *XIAM* code in dealing with low barriers to internal rotation can be overcome with the *BELGI-C_s-2Tops* program, which succeeded to fit the microwave spectra of molecules with C_s symmetry and two methyl tops to experimental accuracy, e.g. methyl acetate [16], ethyl methyl ketone [17], and dimethylbenzaldehyde [18], by adding higher order terms in the Hamiltonian [19]. However, *BELGI-C_s-2Tops* does not include the quadrupole coupling effect. Therefore, we decided to extend the program to a *BELGI-C_s-2Tops-hyperfine* version to treat the microwave spectrum of 45DMTA by taking into account the effect of weak nuclear quadrupole coupling using a first order perturbation approximation.

2. Theoretical part

2.1. Quantum chemical calculations

2.1.1. Geometry optimizations

As other thiazole rings, 45DMTA is planar and aromatic because of the π electron delocalization of the two conjugated double bonds. This constraint confines the structural analysis to have only one starting geometry. Full geometry optimizations were performed on this initial forms using the B3LYP, M06-2X, MP2, and CCSD methods in combination with various Pople and Dunning basis sets [20,21] as implemented in the *GAUSSIAN09* package [22]. The geometry optimized at the MP2/6-311++G(d,p) level of theory is shown in Figure 2 in the principal axes of inertia. The nuclear Cartesian coordinates are given in Table S-1 in the Supplementary Material. Harmonic frequency calculations were carried out to verify whether the stationary point is a saddle point or a true minimum geometry. An interesting feature of 45DMTA is that the dipole moment component in *a*-direction is accidentally almost zero. Therefore, the total dipole moment vector is almost exactly parallel to the *b* principal axis, and we expect a pure *b*-type spectrum.

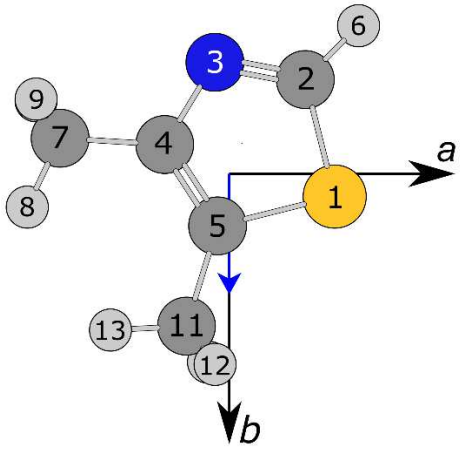

Figure 2: The atom numbering and geometry of 4,5-dimethylthiazole calculated at the MP2/6-311++G(d,p) level of theory, as viewed along the *c* principal axis. The dipole moment is given as a blue arrow. The methyl groups attached to the 4- and 5-ring position are called the 4- and 5-methyl groups, respectively. The hydrogen atom H_{10} is located behind H_9, and H_{14} is behind H_{12}. This figure illustrates that: (i) all heavy atoms are located on the *ab* plane and (ii) the dipole moment is almost exactly parallel to the *b* principal axis with the components of 0.01 D, 1.79 D, and 0.00 D in *a*-, *b*-, and *c*-direction, respectively.

2.1.2. ^{14}N nuclear quadrupole coupling constants

As mentioned in the introduction, 45DMTA contains one ^{14}N nucleus with a nuclear spin of I = 1. Therefore, nuclear quadrupole coupling will result in a hyperfine pattern for each rotational line. The splittings between the hyperfine components depend on the nuclear quadrupole coupling constants (NQCCs). From the optimized structure at the MP2/6-311++G(d,p) level, we carried out a single point electric field gradient calculation at the B3PW91/6-311+(d,p) level of theory using a calibration factor of eQ/h = 4.599 MHz a.u.$^{-1}$ [23]. This combination is a validated method for the prediction of NQCCs in π-conjugated amides in particular and might be also suitable for aromatic rings like 45DMTA. The calculation results in nuclear quadrupole coupling tensors with the diagonal elements χ_{aa} = 0.8070, χ_{bb} = −3.2397, χ_{cc} = 2.4327 MHz, as well as the off-diagonal elements χ_{ab} = −2.1512, χ_{ac} = 0.0117, and χ_{bc} = 0.0028 MHz. Due to the C_s symmetry of the molecule, χ_{ac} and χ_{bc} should be zero. However, since no symmetry constraints were used during the geometry optimizations, a perfect C_s symmetry was not achieved, resulting in small, but non-zero values for these parameters as well as the *c*-coordinates of all heavy atoms given in Table S-1. For comparison, we also performed calculations using the B3PW91/6-311+G(df,pd)//MP2/6-311++G(d,p) combination and the calibration factor of eQ/h = 4.5586(40) MHz a.u.$^{-1}$ [24]. The respective values of the nuclear quadrupole coupling tensor elements are 0.7159, −3.2149, 2.4990, −2.1036, 0.0105, and 0.0030 MHz.

2.1.3. Methyl internal rotations

Beside the ^{14}N nucleus which causes hyperfine splittings of all rotational transitions, 45DMTA features two methyl groups undergoing internal rotation. The resulting torsional fine splittings mainly depend on the orientations of the methyl groups in the molecule, the moment of inertia of the methyl group, and the barriers hindering the internal rotation. While the orientations of the methyl groups and their moments of inertia can be calculated well by geometry optimizations, predicting the barrier heights is a much more difficult task. The predicted values vary in a wide range and depend strongly on the level of theory in use [10,25]. Even within the same molecule, a level that predicts reasonable value for one methyl group may fail for another methyl group [26]. High level quantum chemical methods such as coupled cluster and diffusion quantum Monte Carlo does not directly mean the best agreement with the experiments [27]. However, the magnitude (low, intermediate, or high) of the barrier heights is often correct, which serves as a good starting point for the spectral assignment.

For 45DMTA, we calculated the barrier heights of the methyl groups attached to the 4- and 5-ring position, henceforward called the 4- and 5-methyl groups, respectively, by varying the dihedral angles $\alpha_2 = \angle(N_3,C_4,C_7,H_8)$ and $\alpha_1 = \angle(S_1,C_5,C_{11},H_{12})$, respectively, in a grid of 2° (for atom numbering see Figure 2) with the MP2, B3LYP, M06-2X, and CCSD methods in combination with the 6-311++G(d,p) basis set. All other geometry parameters were optimized. A rotation of only 120° was sufficient due to the three-fold symmetry of the methyl groups. The potential energy curves corresponding to the 4-methyl group are depicted in the left panel of Figure 3, all of which have negligible V_6 contributions. The Fourier coefficients are available in Table S-2 in the Supplementary Material. It is interesting that the barrier height of 158.8 cm^{-1} calculated using the coupled cluster method is similar to that obtained with the much more cost-efficient B3LYP method (165.6 cm^{-1}), but significantly higher than that predicted by MP2 (63.0 cm^{-1}). The value of 98.2 cm^{-1} from calculations with Truhlar's M06-2X method [28] is in between.

In the case of the 5-methyl group, the potential energy curves predicted by the B3LYP, M06-2X, and CCSD methods, illustrated in the right panel of Figure 3, indicate normal three-fold potentials with no V_6 contributions. On the other hand, the MP2 method predicts a considerable V_6 contribution of about 55 % (see Table S-2 in the Supplementary Material for Fourier coefficients). For the 5-methyl group, like for the 4-methyl group, the calculated barrier heights are quite different and vary from about 25 cm^{-1} to 130 cm^{-1}. Again, the B3LYP method yields the highest value, the MP2 method the lowest, and the values from CCSD and M06-2X calculations are almost the mean value of them.

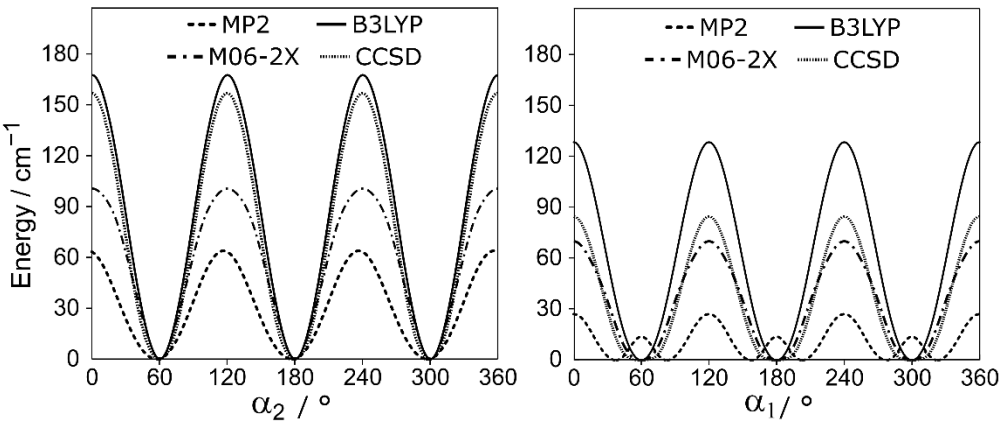

Figure 3: *Left hand side:* The potential energy curves corresponding to a rotation of the 4-methyl group calculated using the MP2, B3LYP, M06-2X, and CCSD methods in combination with the 6-311++G(d,p) basis set. The dihedral angle $\alpha_2 = \angle(N_3,C_4,C_7,H_8)$ is varied over a grid of 2°. *Right hand side:* the respective potential energy curves corresponding

to a rotation of the 5-methyl group by varying the dihedral angle $\alpha_1 = \angle(S_1,C_5,C_{11},H_{12})$. In both figures, energy values relative to the energetically lowest conformation with E_{min} = −646.4816118 (MP2), −647.7803704 (B3LYP), −647.6327793 (M06-2X), and −646.5253342 Hartree (CCSD) are used.

As an alternative, geometry optimizations to a first order transition state of the methyl groups were performed at various levels of theory using the Berny algorithm to calculate the barrier heights [29]. The rotational constants and angles between the internal rotor axes and the principal axes of inertia obtained from geometry optimizations as well as the V_3 potentials from the transition state calculations are collected in Table S-3.

The discrepancy in predicting the methyl barrier heights and especially the abnormally high V_6 contribution in MP2 calculations induced us to perform two-dimensional potential energy surfaces (2D-PES) depending on α_1 and α_2 to study the coupling between the two methyl rotors. The dihedral angles α_1 and α_2 were varied over a grid of 10°. The corresponding energies were parameterized with a 2D Fourier expansion based on terms representing the correct symmetry, which are listed in Table S-4 in the Supplementary Material. Using these Fourier terms, the PES were drawn as a contour plot depicted in Figure 4. All PES indicate significant coupling between the two rotors, shown by the deviation in forms of the minimum regions from circles (oval for calculations using the DFT and CCSD methods, rhomb for the M06-2X method, and double minimum for the MP2 method). The top-top coupling will be revisited in the discussion.

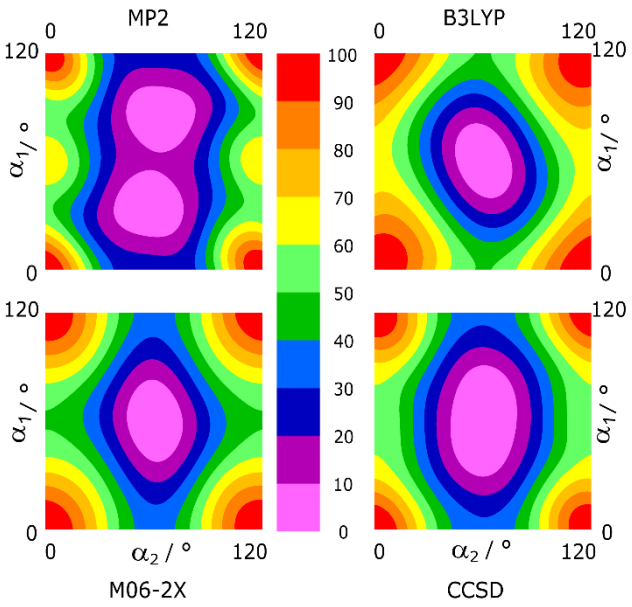

Figure 4: The potential energy surfaces of 45DMTA depending on the rotation of the 4- and 5-methyl groups calculated with the MP2 (top left), B3LYP (top right), M06-2X (bottom left), and CCSD (bottom right) methods and the 6-311++G(d,p) basis set. The dihedral angles $\alpha_1 = \angle(S_1,C_5,C_{11},H_{12})$ and $\alpha_2 = \angle(N_3,C_4,C_7,H_8)$ were varied in 10° steps. The color codes indicate the energy (in percent) relative to the energy minima (0 %) and the energy maxima (100 %).

2.2. The *BELGI-C_s-2Tops-hyperfine* code

The *BELGI-C_s-2Tops* program has been slightly modified to treat hyperfine splittings in the rotational spectrum arising from weak nuclear quadrupole coupling of the nitrogen atom. A perturbation approach has been applied, which is similar to that used first for acetamide (see Eq. 1 of Ref. [30]), then for *N-tert*-butylacetamide (see Eq. 1 of Ref. [31]). The molecular symmetry is C_s in all cases, only the number of rotors increases to two in the present case.

In *BELGI-C_s-2Tops-hyperfine*, like in the *BELGI-C_s-2Tops* code [19], we follow the Hamiltonian initially described by Ohashi et al [32]. The Hamiltonian is set up using a modified Principal Axis Method (PAM) in which the coefficients of the three quadratic rotational operators $(P_xP_y + P_yP_x)$, $(P_yP_z + P_zP_y)$, and $(P_zP_x + P_xP_z)$ are kept fixed to zero in the fit (see Eq. (6) of Ref. [32]). We will refer to it hereafter as the Ohashi-Hougen Hamiltonian. In this Hamiltonian, the nuclear quadrupole interaction terms were also included, taken from the usual form (e.g. Eq. (1) of [30]).

However, the *BELGI-C_s-2Tops-hyperfine* code differs from that in Ref. [32] because it solves the torsion-rotation Hamiltonian in a two-step diagonalization procedure [33], where

the first step deals with the torsion-*K*-rotation part of the problem, and the second step deals with all the rest. This procedure is explained in details in Eq. (3) of Ref. [19] and in Eqs. (1) and (2) of Ref. [18].

In the *BELGI-C_s-2Tops-hyperfine* code, the expectation values of various combinations of angular momentum components $\langle P_a^2\rangle, \langle P_b^2\rangle, \langle P_c^2\rangle,$ and $\langle P_aP_b + P_bP_a\rangle$ are calculated. Subsequently, their numerical values are transferred into the standard hyperfine energy expression:

$$E_{hf}\ (I,J,F) = 2\frac{f(I,J,F)}{J(J+1)}\left[\chi_{aa}\langle P_a^2\rangle + \chi_{bb}\langle P_b^2\rangle - (\chi_{aa}+\chi_{bb})\langle P_c^2\rangle + \chi_{ab}\langle P_aP_b + P_bP_a\rangle\right] \qquad (1)$$

where f (I, J, F) is the Casimir function [34].

The shifts for each rotation-torsion energy level, and therefore those of the hyperfine components, can be calculated using Eq. (1). This enables us to take into account all hyperfine patterns as well as to fit the rotational and rotation-torsional molecular parameters together with the nuclear quadrupole coupling constants in a global fit. The *BELGI-C_s-2Tops-hyperfine* code is currently available by one of the authors (I.K.).

In order to deduce physical meaning from the results of the fit, it is convenient to transform from the quasi-PAM parameters to PAM quantities. The details of the conversion program will be described in detail in section **2.3** below.

2.3 Conversion of the quasi-PAM parameters to PAM quantities

In section 6.1 of Ref. [32], the transformation of the rotation-torsion parameters obtained from the fit in quasi-PAM into PAM quantities is given. However, the transformation of the quadrupole coupling tensor into the principal axis system is not discussed. Here, we will briefly repeat the conversion from quasi-PAM parameters into PAM quantities in the vector-matrix notation, give an algorithm facilitating the transformation, and extend it to the transformation of the quadrupole coupling tensor.

If we focus on the quadratic kinetic energy terms of the Ohashi-Hougen Hamiltonian (Eq. 6 of Ref. [32]), it can be conveniently written as

$$H_{kin}^{(2)} = \boldsymbol{P}^{\dagger}\boldsymbol{M}\boldsymbol{P} \qquad (2)$$

with

$$\boldsymbol{P} = \begin{pmatrix} P_z \\ P_x \\ P_y \\ p_1 \\ p_2 \end{pmatrix}, \quad \boldsymbol{M} = \begin{pmatrix} A' & 0 & 0 & \frac{1}{2}q_1 & \frac{1}{2}q_2 \\ 0 & B' & 0 & \frac{1}{2}r_1 & \frac{1}{2}r_2 \\ 0 & 0 & C' & 0 & 0 \\ \frac{1}{2}q_1 & \frac{1}{2}r_1 & 0 & f_1 & \frac{1}{2}f_{12} \\ \frac{1}{2}q_2 & \frac{1}{2}r_2 & 0 & \frac{1}{2}f_{12} & f_2 \end{pmatrix}.$$

The quantities $A', B', C', f_1, f_2, f_{12}, q_1, q_2, r_1, r_2$ are the parameters obtained from a fit with the *BELGI-C_s-2Tops-hyperfine* code (e.g. see Table 5 of Ref. [19]).

In the same way, the quadratic kinetic energy terms in the classical PAM rigid frame-rigid top Hamiltonian for two internal rotors (Eq.7 of Ref. [32]) can be written as

$$\widetilde{H}_{kin}^{(2)} = \widetilde{\boldsymbol{P}}^{\dagger}\widetilde{\boldsymbol{M}}\widetilde{\boldsymbol{P}} \qquad (3)$$

with

$$\widetilde{\boldsymbol{P}} = \begin{pmatrix} P_a \\ P_b \\ P_c \\ p_1 \\ p_2 \end{pmatrix}, \quad \widetilde{\boldsymbol{M}} = \begin{pmatrix} A'' & Z_{ab} & 0 & Q_1 & Q_2 \\ Z_{ab} & B'' & 0 & R_1 & R_2 \\ 0 & 0 & C'' & 0 & 0 \\ Q_1 & R_1 & 0 & F_1 & F_{12} \\ Q_2 & R_2 & 0 & F_{12} & F_2 \end{pmatrix}$$

and

$$A'' = A + F_1\rho_{1a}^2 + F_2\rho_{2a}^2 + 2F_{12}\rho_{1a}\rho_{2a} \qquad (3a)$$

$$B'' = B + F_1\rho_{1b}^2 + F_2\rho_{2b}^2 + 2F_{12}\rho_{1b}\rho_{2b} \qquad (3b)$$

$$C'' = C \qquad (3c)$$

$$Z_{ab} = F_1\rho_{1a}\rho_{1b} + F_2\rho_{2a}\rho_{2b} + F_{12}(\rho_{1a}\rho_{2b} + \rho_{2a}\rho_{1b}) \qquad (3d)$$

$$Q_1 = -F_1\rho_{1a} - F_{12}\rho_{2a} \qquad (3e)$$

$$Q_2 = -F_2\rho_{2a} - F_{12}\rho_{1a} \qquad (3f)$$

$$R_1 = -F_1\rho_{1b} - F_{12}\rho_{2b} \qquad (3g)$$

$$R_2 = -F_2\rho_{2b} - F_{12}\rho_{1b}. \qquad (3h)$$

We note that in Eq. (3), A'', B'', Z_{ab} are the same as A_{aa}, A_{bb}, and A_{ab} of Eq. (12) from Ref. [32].

The 5-dimensional angular momentum vector $\widetilde{\boldsymbol{P}}$ of the classical PAM Hamiltonian can be transformed to the $\boldsymbol{P}$ vector of the Ohashi-Hougen Hamiltonian by the application of the rotation matrix $\boldsymbol{T}$ (similar to the transformation matrix above Eq. (11) in Ref. [32]).

$$\boldsymbol{P} = \boldsymbol{T}\widetilde{\boldsymbol{P}} \tag{4}$$

with

$$\boldsymbol{T} = \begin{pmatrix} \cos\Theta & -\sin\Theta & 0 & 0 & 0 \\ \sin\Theta & \cos\Theta & 0 & 0 & 0 \\ 0 & 0 & 1 & 0 & 0 \\ 0 & 0 & 0 & 1 & 0 \\ 0 & 0 & 0 & 0 & 1 \end{pmatrix}.$$

Combining Eqs. (2), (3), and (4), we obtain

$$\widetilde{\boldsymbol{M}} = \boldsymbol{T}\boldsymbol{M}\boldsymbol{T}^{-1}. \tag{5}$$

From this transformation, it is obvious that

$$F_1 = f_1, F_2 = f_2, F_{12} = \tfrac{1}{2}f_{12}. \tag{6}$$

Eq. (5) is conveniently evaluated numerically by matrix multiplication for a given rotation angle Θ observing that $\boldsymbol{T}^{-1} = \boldsymbol{T}^{\dagger}$. However, there are only a few discrete angles which are consistent with the equations (3d-h). To find these angles, we vary Θ until consistency is achieved. Therefore, for a given Θ the quantities Q_1, Q_2, R_1, R_2 of $\widetilde{\boldsymbol{M}}$ as given in (3e-h) are used to obtain

$$\rho_{1a} = (Q_2 f_{12} - Q_1 F_2)/U, \quad \rho_{2a} = (Q_1 f_{12} - Q_2 F_1)/U \tag{6a}$$

$$\rho_{1b} = (R_2 f_{12} - R_1 F_2)/U, \quad \rho_{2b} = (R_1 f_{12} - R_2 F_1)/U \tag{6b}$$

with

$$U = F_1 F_2 - F_{12}^2.$$

Then Z_{ab}, also obtained for the given value of Θ, is used to calculate the expression

$$\Delta = Z_{ab} - F_1\rho_{1a}\rho_{1b} + F_2\rho_{2a}\rho_{2b} + F_{12}(\rho_{1a}\rho_{2b} + \rho_{2a}\rho_{1b}). \tag{7}$$

From Eq. (3d) it is clear that $\Delta = 0$ for a properly chosen value of the Θ angle. Therefore, to roughly determine all possible values of Θ, we calculated them in the range $[-\pi, \pi]$ in steps of 0.0001. If for two successive angles Θ_1, Θ_2 the condition $\Delta(\Theta_1) \cdot \Delta(\Theta_2) < 0$ is fulfilled, then there will be an angle Θ between Θ_1 and Θ_2 for which $\Delta = 0$.

Four possible values of Θ were determined that way. Then we refined them to 10^{-9} using the bisection algorithm [35] and obtained $\Theta = 0.016699$ rad, $\Theta + \pi/2$, $\Theta - \pi/2$, and $\Theta - \pi$. Assuming that the coordinate system does not change much, i.e. the *a* axis (PAM) almost corresponds to the *z* axis (quasi-PAM), then only the angle $\Theta = 0.016699$ rad is a physically meaningful solution. The angle with the smallest absolute value was also chosen by Ohashi et al. [32]. The other angles corresponding to the change of the *x* and *z* axes and a rotation of 180°, which will change the directions of the *x* and *z* axes, are also allowed solutions.

Once the transformation of Eq. (5) is carried out with the correct value of Θ, the values for A'', B'', C'' in the matrix $\widetilde{\boldsymbol{M}}$ can be used to determine the structural rotational constants A, B, C from (3a-c).

The direction cosines λ between the internal rotor axes i_1 and i_2 and the inertial *a* and *b* axes are obtained using the equations (8c-d) of Ref. [32] together with $\lambda_{ga}^2 + \lambda_{gb}^2 = 1,\ g = 1,2$. We obtain

$$\lambda_{ga}^2 = \frac{w}{1+w},\ \lambda_{gb}^2 = \frac{1}{1+w} \qquad (8)$$

with

$$w = \left(\frac{I_a \rho_{ga}}{I_b \rho_{gb}}\right)^2 = \left(\frac{B \rho_{ga}}{A \rho_{gb}}\right)^2.$$

From equations (8c-d) of Ref. [32] it is clear that the signs of the direction cosines must be the same as the signs of the corresponding ρ values. The angles between the internal rotor axes and the principal axes of inertia are obtained then with $\angle(i_g, h) = \arccos \lambda_{gh},\ h = a, b, c$.

Once the direction cosines are determined, equations (8c-d) of Ref. [32] also enable us to obtain the moments of inertia of the internal rotors I_g and the corresponding rotational constants F_{0g}.

$$I_g = \frac{I_a \rho_{ga}}{\lambda_{ga}},\ F_{0g} = \frac{\lambda_{ga}}{\rho_{ga}} A. \qquad (9)$$

We also use the rotation matrix $\boldsymbol{T}$ to transform the ^{14}N quadrupole coupling tensor $\boldsymbol{\chi}$ obtained from the *BELGI-C_s-2Tops-hyperfine* fit to the coupling tensor $\widetilde{\boldsymbol{\chi}}$ which refers to the principal axes of inertia.

$$\widetilde{\boldsymbol{\chi}} = \boldsymbol{T}\boldsymbol{\chi}\boldsymbol{T}^{-1} \qquad (10)$$

with

$$\chi = \begin{pmatrix} \chi_{zz} & \chi_{xz} & 0 & 0 & 0 \\ \chi_{xz} & \chi_{xx} & 0 & 0 & 0 \\ 0 & 0 & \chi_{yy} & 0 & 0 \\ 0 & 0 & 0 & 1 & 0 \\ 0 & 0 & 0 & 0 & 1 \end{pmatrix} \quad and \quad \tilde{\chi} = \begin{pmatrix} \chi_{aa} & \chi_{ab} & 0 & 0 & 0 \\ \chi_{ab} & \chi_{bb} & 0 & 0 & 0 \\ 0 & 0 & \chi_{cc} & 0 & 0 \\ 0 & 0 & 0 & 1 & 0 \\ 0 & 0 & 0 & 0 & 1 \end{pmatrix}.$$

2.4. Symmetry considerations

G_{18} is the appropriate molecular symmetry group for 45DMTA which has a frame with C_s point-group symmetry and two inequivalent methyl groups [36,37]. There are different notations to describe the symmetry species of this group. In the Ohashi-Hougen code written to fit the microwave spectrum of *N*-methylacetamide [32], as well as in the *BELGI-C_s-2Tops-hyperfine* code, energy levels are labeled with A (=A_1+A_2), E_1, E_2, E_3, and E_4. Recently, another labeling scheme, for which the G_{18} group is written as the semi-direct product $(C_3^I \otimes C_3^I) \leftthreetimes C_s$, has been introduced for 3,4-dimethylanisole [38] and then applied for 2,4-dimethylanisole [39]. Using this scheme, the torsional species can be labeled by the first part (σ_1,σ_2) of the full symmetry label given in Table 1 of Ref. [38]. We will also use the abbreviated notations (00), (10), (01), (12), and (11) for 45DMTA, where σ_1 and σ_2 represent the 5- and the 4-methyl groups, respectively. The notations A, E_1, E_2, E_3, and E_4 correspond to (00), (10), (01), (12), and (11), respectively.

The seven protons and one nitrogen atom in 45DMTA result in 384 spin functions. The representation of the total nuclear spin function is Γ_{ns}= 96 (00)·A' + 48 (10)·A + 48 (01)·A + 24 (11)·A + 24 (12)·A. The selection rules for torsional components are (00)·A′ ↔ (00)·A″, (10)·A ↔ (10)·A, (01)·A ↔ (01)·A with the spin statistical weight of 96 and (11)·A ↔ (11)·A and (12)·A ↔ (12)·A with the spin weight of 48, showing that if only the spin statistical weight is considered, the intensity of the (11) and (12) torsional components are only half of that of the other species.

3. Microwave spectrum

3.1. Experimental setup

The sample of 45DMTA was purchased from TCI Deutschland GmbH, Eschborn, Germany, with a stated purity of over 97% and used without further purification. The rotational spectra were measured using a COBRA-type pulsed molecular jet Fourier transform microwave spectrometer covering the frequency range from 2.0 to 26.5 GHz [40]. The sample was placed

on a piece of a pipe cleaner as carrier material, which was inserted in a stainless steel tube close to the nozzle. Helium at a pressure of approximately 200 kPa flowed over the sample and the resulting 45DMTA-helium mixture was expanded into the Fabry-Pérot cavity.

To obtain the spectrum, the time domain signal was Fourier transformed. In our spectrometer, the supersonic jet and the resonator are coaxially aligned. Thus, each rotational transition is split into two components due to the Doppler effect. The rest frequency is calculated as the arithmetic mean of the frequencies of the Doppler components. The line widths are approximately 15-30 kHz for isolated lines. However, we observed additional splittings in the order of more than 10 kHz in many transitions, which are probably caused by spin-spin or spin-rotation coupling. Therefore, the estimated measurement accuracy is about 4 kHz.

3.2. Spectral analysis

The dipole moment components predicted at the MP2/6-311++G(d,p) level of theory are 0.01 D, 1.79 D, and 0.00 D in *a*-, *b*-, and *c*-direction, respectively. Because of the negligible components in *a*- in *c*-direction, we expect a pure *b*-type spectrum for 45DMTA.

Preliminary predictions of the spectrum using a rigid-rotor Hamiltonian were based on the rotational constants calculated at the MP2/6-311++G(d,p) level of theory given in Table S-3 of the Supplementary Material. A broadband scan in the frequency range 9.00 – 13.25 GHz was automatically recorded as overlapping spectra in steps of 0.25 MHz. It revealed a very dense spectrum, which made the assignment quite challenging. We searched first for the *b*-type $J{+}1_{0,J+1} \leftarrow J_{1,J}$, $J{+}1_{1,J+1} \leftarrow J_{0,J}$, and $J{+}1_{1,J} \leftarrow J_{2,J-1}$ lines with J ranging from 2 to 4. The (00) torsional state of these transitions could be identified by trial and error, which allowed us to predict other (00) lines well.

All rotational lines show hyperfine structures, as can be seen in Figure 5, due to the quadrupole coupling of the ^{14}N nucleus. As a next step, this effect was taken into account. Using the NQCCs calculated in section 2.1.2, the hyperfine structures of the (00) torsional state were readily assigned. A fit using a rigid-rotor model with centrifugal distortion correction and first order approximation for the quadrupole coupling yielded molecular parameters with sufficient accuracy.

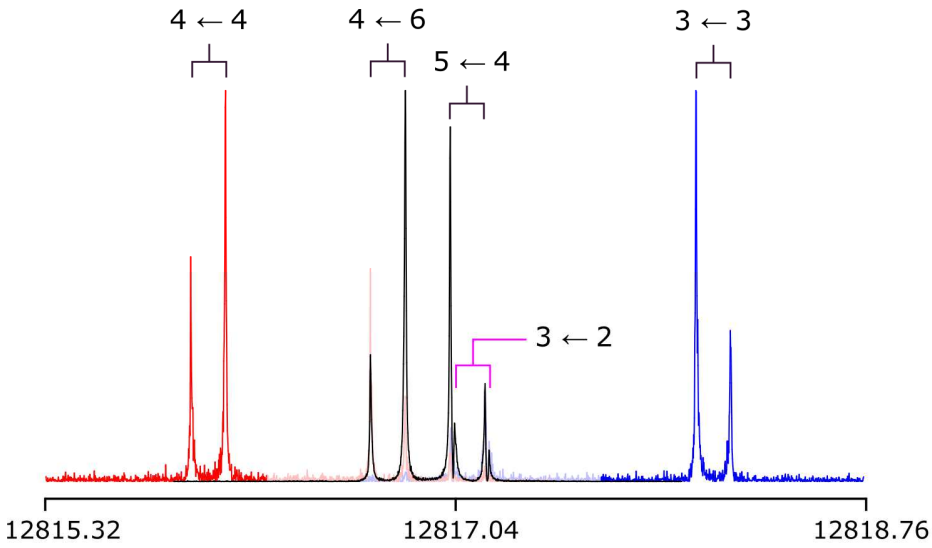

Figure 5: Typical spectra of the (11) torsional species of the $4_{14} \leftarrow 3_{03}$ transition of 45DMTA recorded at high resolution. The frequencies are in MHz. The quadrupole components are given by F' ← F; the Doppler pairs are marked by brackets. Three spectra are illustrated and can be distinguished by different colors. For each spectrum, 50 decays were co-added.

After excluding all (00) lines, an amount of approximately four times of the assigned lines remain in the broadband scan. They belong to the other torsional species arising from the internal rotations of the two methyl groups. The program *XIAM* [12] was used to predict the torsional splittings. The initial values of the angles between the internal rotor axes and the principal axes of inertia as well as the hindering potentials were taken from *ab initio* calculation at the MP2/6-311++G(d,p) level of theory, those of the rotational constants, the centrifugal distortion constants, and the NQCCs from the rigid-rotor fit. The (01) and (10) species were assigned after a lot of trial and error, and we were able to get a satisfactory fit including the (00), (01), and (10) torsional species with their hyperfine components. However, we failed to assigned any (11) and (12) species with the prediction using molecular parameters from this fit.

In figure 6, a portion of the broadband spectrum with the $4_{04} \leftarrow 3_{13}$ and $4_{14} \leftarrow 3_{03}$ rotational transitions is given as an example. It shows that the splitting between the (10), (11), and (12) torsional species is rather small for some transitions, resulting in a triplet pattern. This gave us a hint to identify the (11) and (12) lines. Using the fit in which the (00), (01), and (10) lines are included with sufficient accuracy, all lines belong to those species were marked in the broadband scan. The remaining lines belong to the triplet were then identified as (11) and (12) lines of the same rotational transition as (10) in the same triplet.

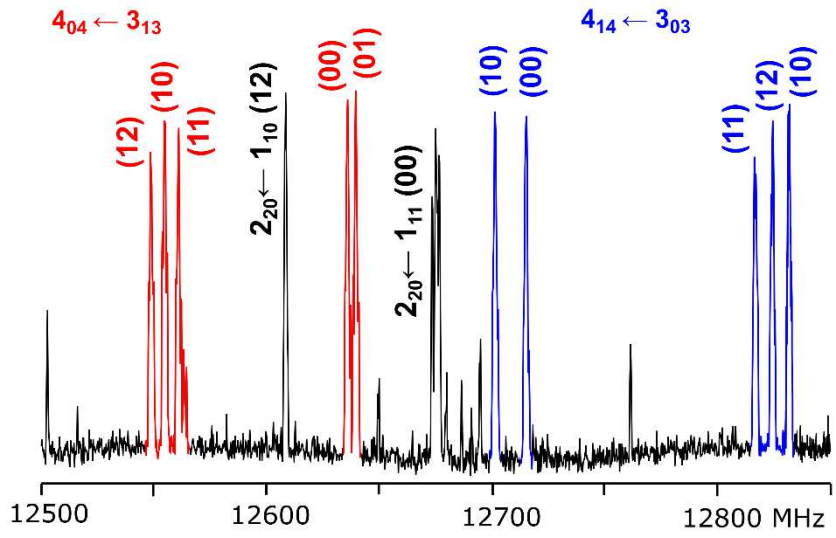

Figure 6: A portion of the spectrum of 45DMTA showing the five torsional components (00), (10), (01), (11), and (12) of the $4_{04} \leftarrow 3_{13}$ (in red) and $4_{14} \leftarrow 3_{03}$ (in blue) rotational transitions. Two other intense lines (in black) are marked with their torsional species and rigid rotor quantum numbers *J, K_a, K_c*. The lines are broadened or split because of the quadrupole coupling arising from the ^{14}N nucleus.

Despite the fact that we were successful to find some (11) and (12) lines within the broadband scan range, the molecular parameters obtain from the *XIAM* fit, where all five torsional species were included, did not yield satisfactory results at this stage. Therefore, we were not able to assign any further (11) and (12) lines out of the range of the broadband scan. To overcome this problem, the (10) species, corresponding to the $\sigma = 1$ state of the 5-methyl group with lower barrier, had to be excluded, and we performed two separated fits, one with the (00), (01), (11) and the other with the (00), (01), and (12) species. With the predictions from these two fits, we were able to extend considerably the assignment of the (11) and (12) torsional species. The hyperfine structure analysis of the (10), (01), (11), and (12) species was straightforward. The frequency list is available in Table S-4 in the Supplementary Material.

As can be seen in the frequency list, there are some *c*-type perturbation allowed transitions and some transitions which are neither *a*-, *b*-, nor *c*-type. It is not a surprise because the quantum numbers K_a and K_c have no meaning for the symmetry of the rotational transitions apart from the (00) species. In all other species, the K_a, K_c quantum numbers just indicate the order of energy in analogy to the asymmetric top energy level. One interesting point is that though the value of the dipole moment in the *a*-direction is almost zero, we could still observe the (00) component of one *a*-type transition, $4_{14} \leftarrow 3_{13}$, with its hyperfine structure.

4. Results of the Fits

A total of 315 rotational transitions with 1009 hyperfine components were assigned and fitted using the *XIAM* and the *BELGI-C_s-2Tops-hyperfine* codes, treating two methyl internal rotations and a weakly coupling quadrupole nucleus. While the *XIAM* fit gives a root-mean-square (rms) deviation of 399.8 kHz, the *BELGI-C_s-2Tops-hyperfine* fit offers a satisfactory rms deviation of 4.2 kHz. The coverage of the data and the quality of the fits are shown in Table 1. The molecular parameters from the *XIAM* fit and the results from *ab inito* calculation at the MP2/6-311++G(d,p) level of theory are given in Table 2. For comparison, parameters from the *BELGI-C_s-2Tops-hyperfine* fit which have been transformed into the PAM system are also listed in Table 2. The *BELGI-C_s-2Tops-hyperfine* parameters in the quasi-PAM system are shown in Table 3.

Table 1. Overview of the data set coverage and fit qualities for 45DMTA.

Γ^a	$(\sigma_1\sigma_2)$	$N_{hf}{}^b$	$N_t{}^c$	rms^d	$J_{max}{}^e$	$K_{max}{}^f$
A	(00)	214	68	2.9	9	7
E_1	(10)	209	66	6.3	8	6
E_2	(01)	212	68	4.0	9	6
E_3	(12)	180	58	3.5	7	6
E_4	(11)	194	55	3.5	7	5
XIAM fit		1009	315	399.8	9	7
BELGI fit		1009	315	4.2	9	7

[a] Symmetry species of the lines in each row.
[b] Number of hyperfine components in the torsional data group.
[c] Number of torsional components in each data group.
[d] Root-mean-square deviation of each data group in kHz.
[e] Largest J and K_a values in each data group.

Using *XIAM*, the rotational constants, the centrifugal distortion constants, and the nuclear quadrupole coupling constants can be obtained. The internal rotation parameters which are the V_3 hindering potentials, the angles between the internal rotation axes and the principal *a*-axis, the higher order parameters D_{pi2K}, D_{pi2J} and D_{pi2-} (for definition, see Ref. [41]) were also determined from the fit. A fit without any top-top coupling parameters was performed first, where the rms deviation was about 4.2 MHz. Since the 2D-PES, given in section 2.1.3, indicated possible couplings between the two methyl groups, we attempted to reduce the rms deviation by including the top-top coupling parameter V_{cc}, multiplying the

cosine terms of the two tops. The rms decreases by approximately 10 times to 399.8 kHz. However, the parameters are highly correlated. All attempts to reduce the rms deviation by fitting another top-top coupling parameter including the sine terms, V_{ss}, were not successful. We note that the sign of D_J should be positive, which is confirmed by the results of the *BELGI* fit given in Tables 2 and 3. The negative value obtained with *XIAM* might arise from the large rms deviation. Consequently, the deduced centrifugal distortion constants are not physically meaningful. The D_J constant is contaminated by the internal rotation effects which are insufficiently described with *XIAM* and becomes an effective parameter which no longer presents the effect of centrifugal distortion. Furthermore, because only transitions in the ground torsional state are included, there are strong correlations between the V_3 potentials and I_g. Therefore, the I_g values of both methyl groups were fixed to the calculated values, which correspond to F_{0g} values of 160 GHz.

Table 2. Molecular parameters of 45DMTA referred to the inertial principal axis system (PAM) obtained by the programs *XIAM* and *BELGI-C_s-2Tops-hyperfine* as well as from *ab initio* calculation at the MP2/6-311++G(d,p) level of theory .

Parameter[a]	Unit	*XIAM*	*BELGI*	*ab initio*[b]
A	GHz	3.187379(11)	3.10317(73)	3.177
B	GHz	2.457116(11)	2.462464(91)	2.448
C	GHz	1.4116299(57)	1.41137155(90)	1.407
D_J	kHz	–0.348(83)	0.0953(27)	0.1220
D_{JK}	kHz	2.52(29)		0.4159
D_K	kHz	–2.01(37)		-0.1047
d_1	kHz	0.093(40)		-0.04370
d_2	kHz	–0.094(16)		-0.002793
$V_{3,1}$	cm^{-1}	61.697(19)	71.007(38)	27.2
ρ_1	unitless	0.015900[c]	0.015744(11)	0.0154618
$F_{0,1}$	GHz	160[d]	161.3(12)	160
F_1	GHz	162.580[c]	161.2419[d]	162.9108
$\angle(i_1,a)$	°	108.9544(7)	109.149(24)	106.98
$\angle(i_1,b)$	°	18.9544(7)	19.149(24)	16.98
$\angle(i_1,c)$	°	90[e]	90[e]	89.98
$D_{pi2J,1}$	kHz	63.7(25)		
$D_{pi2K,1}$	MHz	–0.5882(46)		
$D_{pi2-,1}$	kHz	140.7(19)		
$V_{3,2}$	cm^{-1}	126.543(13)	131.524(69)	64.3
ρ_2	unitless	0.019891[c]	0.018990(23)	0.0194656

$F_{0,2}$	GHz	160[d]	163.23(21)	160
F_2	GHz	163.251[c]	160.7439[d]	163.089986
$\angle(i_2,a)$	°	175.0838(40)	175.661(13)	176.64
$\angle(i_2,b)$	°	94.9162(40)	94.339(13)	93.36
$\angle(i_2,c)$	°	90[e]	90[e]	89.99
$D_{pi2J,2}$	kHz	45.3(57)		
$D_{pi2K,2}$	MHz	–0.671(11)		
$D_{pi2-,2}$	kHz	90.2(42)		
F_{12}	GHz	0.8630[c]	0.0433(99)	0.88
	cm^{-1}	0.0288[c]	0.00145(33)	0.0294
V_{cc}	cm^{-1}	–4.765(12)	–5.294(12)	5.5
V_{ss}	cm^{-1}		–13.14(20)	
χ_{aa}	MHz	0.55(12)	0.5401(13)	0.8070
χ_{-}[f]	MHz	–5.71(16)	–5.6659(29)	–5.6724
χ_{ab}	MHz	–2.04(23)	–2.2358(24)	–2.1512
rms[g]	kHz	399.8	4.2	
N[h]		1009	1009	

[a] All parameters refer to the principal axis system. Watson's S reduction and I[r] representation was used. [b] Centrifugal distortion constants obtained by anharmonic frequency calculation at the MP2/6-311++G(d,p) level of theory. The rotational constants of the vibrational ground state are A = 3.161 GHz, B = 2.432 GHz, and C = 1.399 GHz. NQCC values obtained at the B3PW91/6-311+(d,p)//MP2/6-311++G(d,p) level. [c] Derived parameters. [d] Fixed parameter. [e] Fixed due to symmetry. [f] $\chi_{-} = \chi_{bb} - \chi_{cc}$. [g] Root-mean-square deviation of the fit. [h] Number of hyperfine components.

Using the same data set the *BELGI-C_s-2Tops-hyperfine* code floated 37 parameters, which are the three rotational constants *A, B, C*, five quartic centrifugal distortion constants, the NQCCs χ_{aa}, χ_{bb}, and χ_{ab} in Eq. (1), the r_1 and r_2 parameters multiplying the off-diagonal $P_x p_2$ and $P_x p_1$ terms, respectively, the potential barrier heights for each top V_{31} and V_{32}, the rotation-torsion coupling term q_1 and q_2 (which are related to the ρ_1 and ρ_2 constants). Fifteen higher order terms were also determined representing the rotation-torsion interaction beyond the rigid top-rigid frame model, and finally five terms corresponding to the top-top interaction (V_{12cc}, V_{12ss}, F_{12}, B_{12}, r_{12P}). At the beginning, we also tried to fit the two reduced internal rotational constants F_1 and F_2, but the rms deviation of the fit did not significantly decrease and the parameters were highly correlated, as it is often the case when the data set only contains transitions from the ground torsional state. The F_1 and F_2 parameters were then fixed to values obtained when they were floated. We note that $F_g = \frac{F_{0g}}{r_g}$ with $r_g = 1 - I_g\left(\frac{\lambda_{ga}^2}{I_a} + \frac{\lambda_{gb}^2}{I_b}\right)$. The rms deviation of the *BELGI-C_s-2Tops-hyperfine* fit is 4.2 kHz, which is almost the measurement accuracy.

Table 3. Molecular parameters of 45DMTA referred to the quasi-PAM axis system obtained by the program *BELGI-C_s-2Tops-hyperfine*.

Operator[a]	Par.[b]	Program[c]	Unit	Value[d]
P_z^2	*A*	*OA*	GHz	3.16755(72)
P_x^2	*B*	*B*	GHz	2.496028(75)
P_y^2	*C*	*C*	GHz	1.41137155(90)
$-P^4$	Δ_J	*DJ*	kHz	0.0953(27)
$-P^2P_z^2$	Δ_{JK}	*DJK*	kHz	1.047(32)
$-P_z^4$	Δ_K	*DK*	kHz	–5.051(46)
$-2P^2\left(P_x^2-P_y^2\right)$	δ_J	*ODELN*	kHz	0.0322(13)
$-\left\{P_z^2,\left(P_x^2-P_y^2\right)\right\}$	δ_K	*ODELK*	kHz	0.2172(38)
$(1/2)(1-cos\alpha_1)$	$V_{3,1}$	*V31*	cm^{-1}	71.007(38)
$(1/2)(1-cos\alpha_1)\{P_z,P_x\}$	$V_{3,1AB}$	*V31AB*	MHz	–14.558 (77)
p_1^2	f_1	*F1*	GHz	161.2419[e]
$p_1^2P^2$	f_{1J}	*F1J*	MHz	–1.1211(54)
P_zp_1	q_1	*Q1*	GHz	2.1144(21)
$P_z^3p_1$	q_{1K}	*Q1K*	MHz	–0.03949(20)
P_xp_1	r_1	*R1*	GHz	–4.6166(36)
$(1/2)\{P_z^2,P_x\}p_1$	r_{1K}	*R1K*	MHz	0.02734(23)
$p_1^2P_x^2$	B_1	*B1*	MHz	0.830(23)
$p_1^2P_y^2$	C_1	*C1*	MHz	0.9544(55)
$(1/2)(1-cos\alpha_2)$	$V_{3,2}$	*V32*	cm^{-1}	131.524(69)
$(1/2)(1-cos\alpha_2)\ P^2$	$V_{3,2J}$	*V32J*	MHz	–4.956 (77)
$(1/2)(1-cos\alpha_2)\ P_z^2$	$V_{3,2K}$	*V32K*	MHz	198.6(14)
$(1/2)(1-cos\alpha_2)\{P_z,P_x\}$	$V_{3,2AB}$	*V32AB*	MHz	5.10(25)
$(1/2)(1-cos\alpha_2)\left(P_x^2-P_y^2\right)$	$V_{3,2BC}$	*V32BC*	MHz	–6.423(76)
p_2^2	f_2 [e]	*F2*	GHz	160.7439
$p_2^2P_z^2$	f_{2K}	*F2K*	MHz	8.299(66)
P_zp_2	q_2	*Q2*	GHz	6.0878(75)
$P_z^3p_2$	q_{2K}	*Q2K*	MHz	0.4181(32)
P_xp_2	r_2	*R2*	GHz	0.46744(72)
$(1/2)\{P_z^2,P_x\}p_2$	r_{2K}	*R2K*	MHz	0.2741(28)
$p_2^2P_x^2$	B_2	*B2*	MHz	–0.3179(92)
$p_2^2P^2P_z^2$	Δ_{2JK}	*DEL2JK*	kHz	–0.278(11)
$sin3\alpha_1 sin3\alpha_2$	V_{12S}	*V12S*	cm^{-1}	–13.14(20)

$(1-cos3\alpha_1)(1-cos3\alpha_2)$	V_{12C}	*V12C*	cm^{-1}	–5.294(12)
p_1p_2	f_{12}[f]	*F12*	cm^{-1}	0.00289(66)
$p_1p_2(p_1+p_2)P_x$	r_{12P}	*R12P*	MHz	–4.666(74)
$p_1p_2P_x^2$	B_{12}	*B12*	MHz	–0.0700(47)
	$2\chi_{aa}$[g]	*XAA*	MHz	0.6137(13)
	$2\chi_{bb}$[g]	*XBB*	MHz	–3.1766(13)
	$2\chi_{ab}$[g]	*XAB*	MHz	–2.1716(24)
	rms[h]		kHz	4.2
	N[i]			1009

[a] Operator which the parameter multiplies in the program. α_1 and α_2 correspond to the 5- and the 4-methyl groups, respectively. {u, v} is the anti-commutator uv + vu.

[b] Notation of Eq. (6) and Table 3 of Ref. [32], except for *A*, *B*, and *C*, where the prime was removed.

[c] Notation used in the program input and output.

[d] Value of the parameter obtained from the final least-squares fit, with one standard uncertainty given in parentheses.

[e] Fixed to values obtained in a previous fit.

[f] Note that $F_{12} = \frac{1}{2}f_{12}$, as given in Eq. (6).

[g] Hyperfine energies were calculated using Eq. (1) of Refs. [30,34]

[h] Root-mean-square deviation of the fit.

[i] Number of hyperfine components.

5. Discussion

5.1. Quality of the fits

The fit given as Fit *XIAM* in Table 2 has an rms deviation of 399.8 kHz, which is 100 times the estimated measurement accuracy of 4.0 kHz. This can be explained by the relatively low hindering potentials of both methyl groups and the rather significant coupling between the two tops. Similar deviations have been found in many one-top problems with similar barrier heights treated by the program *XIAM*, i.a. ethyl acetate (101.606(23) cm^{-1}, 85.3 kHz) [42], allyl acetate (98.093(12) cm^{-1}, 54.0 kHz) [43], and vinyl acetate (151.492(34) cm^{-1}, 92.3 kHz) [44]. If top-top coupling is present, as in the case of pinacolone, the rms deviation determined by *XIAM* is even worse (121.532(57) cm^{-1}, 1155.8 kHz) [45].

We notice that the rms value can be reduced from 399.8 kHz to about 350 kHz by fitting F_{12}. However, this rms value is still not comparable to the measurement accuracy. Thus, we decided to keep this parameter as a derived parameter rather than floating it in the *XIAM* fit since it is correlated with other parameters in the fit. The *XIAM* fit presented in Table 2 follows a model considering two molecular subunits (the top and the frame) with fixed geometries and fixed dihedral angles describing the orientation of these subunits within the molecule. Indeed, very few higher order terms in *XIAM* allow for distortion from this rigid frame-rigid top model. Therefore, the value of F_{12} derived from the *XIAM* fit fairly matches the one calculated at the MP2/6-311++G(d,p) level of theory which also corresponds to a

rigid frame-rigid top model. On the other hand the F_{12} value obtained by *BELGI-C_s-2Tops-hyperfine* is 20 times smaller than the value from the *XIAM* fit (see Table 2). This is probably due to the different approach used in the *BELGI-2Tops-hyperfine* code, where f_{12} is an effective parameter with a different meaning compared to that from the rigid top-rigid rotor model. Fifteen higher order terms have to be used in the *BELGI-C_s-2Tops-hyperfine* code in order to achieve the measurement accuracy. Those higher order terms allow for various distortion and Coriolis effects.

5.2. Geometry parameters

The rotational constants obtained from the *XIAM* fit differ from the values calculated at the MP2/6-311++G(d,p) level of theory by –0.33% for *A*, –0.37% for *B*, and –0.33% for *C* (with respect to the *XIAM* values). This result matches well with our expectation for the level of theory in use. Since the rotational constants from the *XIAM* fit are deduced from the vibrational ground state and the results obtained from the *ab initio* calculations refer to the molecular equilibrium values, they are not directly comparable. The rotational constants in the vibrational ground state obtained from anharmonic frequency calculations given in the footnote of Table 2 are not in better agreement with the experimental values with deviations of –0.82% for *A*, –1.02 % for *B* and –0.89% for *C*. In general, the rotational constants are predicted well with various combinations of method and basis set (see Table S-3 in the Supplementary Material). The MP2/6-311++G(d,p) level of theory yielded good results for 45DMTA and is therefore recommended for substituted thiazoles. Results from calculations using the more cost-efficient Truhlar's method or B3LYP method are also satisfactory.

While the *B* and *C* constants determined from *XIAM* and *BELGI-C_s-2Tops-hyperfine* are essentially similar with deviation of only 0.22% and –0.02%, respectively, the A rotational constants differ by –2.64% (with respect to the *XIAM* values). Due to symmetry, the *C* constant should be the same in *XIAM* and *BELGI-C_s-2Tops-hyperfine*. The small deviation of –0.02% for the *C* constant can be explained by the contamination from higher order terms. The significant difference on the *A* rotational constant between the *XIAM* and the *BELGI*-family codes has been frequently observed in previous work [17,46,47]. The centrifugal distortion constants are not well-determined in the *XIAM* fit (probably because of the limitation on the maximum *J* and *K* values accessible in our experiments and the large rms deviation of the fit) and those from *BELGI-C_s-2Tops-hyperfine* in the quasi-PAM system are not comparable with the values calculated using anharmonic frequency calculations.

The conjugated π electron system in thiazoles and oxazoles causes the planarity of the molecules, which is directly associated with the aromaticity. In the cases of thiazole and oxazole, the inertial defect $\Delta_c = I_c - I_a - I_b$ is almost zero with a value of 0.074 [3] and 0.056 uÅ^2 [48], respectively, where I_a, I_b, I_c are the principal moments of inertia. In the cases of mono-methyl substituted derivatives, we obtained inertial defects close to 3.2 uÅ^2 caused by two out-of-plane hydrogen atoms, which are, e.g., –3.059, –3.092, and –3.077 uÅ^2 for n-methylthiazole (n = 2 (**1**), 4 (**2**), 5 (**3**), respectively, for molecule numbering see Figure 1) [4-6] as well as –3.127, –3.100, and –3.121 uÅ^2 for n-methyloxazole (n = 2 (**5**), 4 (**6**), 5 (**7**), respectively) [7,8]. In 45DMTA, there are two methyl substitutions with two pairs of out-of-plane hydrogen atoms, leading to an inertial defect of 6.4 uÅ^2. This is similar to the values of –6.275, –6.280, –6.469, and –6.508 uÅ^2 found for 2,5-dimethylthiophene [10], 2,5-dimethylfuran [11], and *trans* and *cis*-2-acetyl-5-methylfuran [26], respectively, which are also aromatic five-membered rings possessing two methyl groups.

5.3. ^{14}N nuclear quadrupole coupling constants

The experimentally deduced ^{14}N NQCCs from both *XIAM* and *BELGI* fits are in very good agreement. Calculated values obtained using the combination B3PW91/6-311+G(d,p)//MP2/6-311++G(d,p) recommended for formamides possessing conjugated π-electron systems [23] are sufficiently accurate for the assignment. This combination also yielded satisfactory results for some other aromatic rings such as benzonitrile [49] and 2-methylpyrrole [50]. However, in this particular case of 45DMTA, values from calculations using the traditional combination B3PW91/6-311+G(df,pd)//MP2/6-311++G(d,p), which performs better for aliphatic formamides, are slightly closer to the experimental values.

In thiazole, monomethyl thiazoles, and 45DMTA, the principal *c*-axis is perpendicular to the ring plane. Therefore, it is collinear with one principal axis of the coupling tensor, enabling direct comparison of the χ_{cc} components. A summary of the ^{14}N coupling constants χ_{cc} is also presented in Figure 1. The value of 2.41 MHz found for thiazole (**1**) [3] is essentially the same as that of 2.390 MHz for 2-methylthiazole (**2**) [4], indicating that methylation effect on χ_{cc} can be almost neglected (for molecule numbering see Figure 1). Comparison of the χ_{cc} value for different nitrogen containing heterocycles and their mono-methyl derivatives confirms this conclusion [50]. Surprisingly, in 4- (**3**) and 5-methylthiazole (**4**), the value of χ_{cc} increases significantly to 2.539 and 2.711 MHz, respectively. The χ_{cc} value found in 45DMTA (**5**) lies in between the values of χ_{cc} in 4-methylthiazole (**3**) and 5-

methylthiazole (**4**). Obviously, the +I effect of methyl groups [51] play a significant role for the π electron distribution within the ring, which also contributes to the unexpected low barriers to internal rotation of the methyl groups and the different electronic surrounding of the nitrogen nucleus. This might also explain the better performance of the B3PW91/6-311+G(df,pd)//MP2/6-311++G(d,p) over the B3PW91/6-311+G(d,p)//MP2/6-311++G(d,p) combination.

5.4. Methyl torsional barriers

As can be seen in Figure 1, the barriers to internal rotation of 357.55(14) cm^{-1} and 332.02(81) cm^{-1} found for the methyl groups in 4- (**3**) [5] and 5- methylthiazol (**4**) [6], respectively, are very similar. In the case of 45DMTA (**5**), we expected higher values of this parameter due to sterical hindrance, as previously observed in aromatic six-membered rings such as 3,4-dimethylbenzaldehyde [18], 3,4-dimethylanisole [38], and *o*-xylene [52] (about 500 cm^{-1} in all cases). Surprisingly, the experimentally deduced barrier height decreases drastically to 61.697(19) cm^{-1} for the 5-methyl and 126.543(13) cm^{-1} for the 4-methyl group. A similar situation has been observed in 2,3-dimethylanisole [53], where the barrier height of the *o*-methyl group featuring the highest sterical hindrance is only about 27 cm^{-1}, while the value for its neighboring *m*-methyl group is 518.7(12) cm^{-1}. In a work on methyl substituted naphthalenes, Schnitzler et al. reported that the barrier of the methyl internal rotation in 1-methylnaphthalene is so high, that the torsional splittings are not resolvable in the spectrum [54]. This usually corresponds to a value of approximately 1000 cm^{-1} or higher value of the barrier to internal rotation. If a methyl group is added in the close proximity, as in the case of 1,2-dimethylnaphthalene, the barrier height of the 1-methyl group decreases remarkably to 306.96(25) cm^{-1}, while the value of the 2-methyl group increases from 227.12(42) cm^{-1} (found for 2-methylnaphthalene) to 437.95(75) cm^{-1} [54]. We believe that the low torsional barriers observed for the two methyl groups of 45DMTA as well as for the 1-methyl group of 1,2-dimethylnaphthalene can be explained similarly as for the *o*-methyl group of 2,3-dimethylanisole. Following the atom numbering in Figure 2, and assuming that the electronic environment of the C_5 atom and its methyl group would be exactly the same as the one around the N_3 atom, the local frame symmetry of the 4-methyl group would be C_{2v} and therefore, the leading term in the expansion of the potential function would no longer be V_3 but V_6. In reality, the C_5 atom and its methyl group have a different electronic environment compared to

the N_3 atom. Thus, the frame symmetry is slightly out-of-balance, resulting in a small V_3 contribution.

The same explanation can also be applied for the 5-methyl group. The higher barrier found for the 4-methyl group compared to that of the 5-methyl group, can be due to the fact that the electronic surrounding for one carbon atom with an attached methyl group is more similar to that for a sulfur atom than that for a nitrogen atom. The closer one is to a C_{2v} symmetry, the lower the barrier will be.

Quantum chemical calculations at all levels of theory in use result in a V_3 potential barrier lower for the 5-methyl group than for the 4-methyl group (see Figure 3). This is in agreement with the experimental results. However, the value of this parameter for each top varies strongly depending on the level of theory (for the 4-methyl group between 16 and 272 cm^{-1} and for the 5-methyl group between 24 and 174 cm^{-1}). Currently, attempts to find a level of theory which yields sufficiently accurate V_3 potential value to satisfy the experimental data are still not successful, and predicting the barriers to internal rotation remains a difficult task.

The V_6 contribution in the potential barrier of the 5-methyl group could not be determined with the current data set. Therefore, the significant contribution of over 50% found in calculations at the MP2/6-311++G(d,p) level cannot be validated experimentally.

While the barrier to internal rotation of 126.543(13) cm^{-1} of the 4-methyl group deduced from the *XIAM* fit is in agreement with the value of 131.524(69) cm^{-1} from *BELGI-2Tops-C_s-hyperfine*, the value of the 5-methyl group differs by approximately 10 cm^{-1} (see Table 2). The differences might be caused by effects absorbed into the torsional barriers which are accounted for by the high order parameters fitted in *BELGI-C_s-2Tops-hyperfine* but not treated in *XIAM*.

5.5. Top-top coupling

The value of the top-top potential coupling constant V_{12c}, multiplying the $(1 - \cos 3\alpha_1)(1 - \cos 3\alpha_2)$ operator, is −4.765(12) cm^{-1} and −5.294(12) cm^{-1} in the *XIAM* and *BELGI-C_s-2Tops-hyperfine* fits respectively, i.e. about 7 % of the $V_{3,1}$ potential barrier height for the 5-methyl group and close to the value of −3.5 cm^{-1} found for methyl acetate [19]. The value found for the closely related constant V_{12s}, multiplying $\sin 3\alpha_1 \cdot \sin 3\alpha_2$, is −13.14(20) cm^{-1}, larger than that of V_{12c}.

The value and sign of V_{12c} obtained from the *XIAM* fit agrees well with those of the *BELGI* fit, while V_{12s} cannot be determined by *XIAM*. Table 2 and 3 show that the effects associated with this top-top torsional mode coupling near the equilibrium configuration are actually larger in 45DMTA than in methyl acetate [19], since the difference $|V_{3,1} - V_{3,2}|$ is about 61.5 cm^{-1}, while V_{12s} is only about −13 cm^{-1}.

6. Conclusion

The microwave spectrum of 45DMTA with five torsional species and ^{14}N quadrupole hyperfine splittings were recorded under molecular jet conditions and successfully assigned assisted by quantum chemistry. In total, 97 rotational transitions with 315 torsional and 1009 quadrupole hyperfine components were identified and highly accurate molecular parameters were determined using the programs *XIAM* und *BELGI-C_S-2Tops-hyperfine*. While the fitting procedure was a challenge for *XIAM*, *BELGI-C_S-2Tops-hyperfine* could reduce the rms deviation by a factor of approximately 100 times down to 4.2 kHz, a value close to the measurement accuracy. In contrast to the intermediate barriers found for the respective monomethyl derivatives (357.6 cm^{-1} for 4-methylthiazole and 332.0 cm^{-1} for 5-methylthiazole) and in spite of steric hindrance, the torsional barriers of both methyl groups in 45DMTA are low (126.543(13) cm^{-1} for the 4-methyl group and 61.697(19) cm^{-1} for the 5-methyl group). This is most probably due to potential coupling between the two methyl groups arising from motions with an anti-geared character. Methylation at the fourth and/or fifth position(s) significantly influence(s) the π electron distribution within the ring, resulting in different electronic surroundings for the nitrogen nucleus and higher values of the χ_{cc} component of the quadrupole tensor.

Acknowledgments

We thank Dr. Alexandra Welzel for the results from her Ph.D. thesis entitled “Bau einer heizbaren Ultraschalldüse zur mikrowellenspektroskopischen Untersuchung schwerflüchtiger Substanzen im Molekularstrahl” at the RWTH Aachen University. V.V. thanks the Fonds der Chemischen Industrie (FCI) and T.N. the Université de Paris for a Ph.D. fellowship. Simulations were performed with computing resources granted by JARA-HPC from the RWTH Aachen University under the project jara0124. This work is supported by the Agence Nationale de la Recherche ANR (project ID ANR-18-CE29-0011).

References

[1] M.J. Wilbym P.J. Hutchinson, CNS Drug Rev. 10 (2004) 281–294.

[2] E. Beltrán-Partida, B. Valdez-Salas, E. Valdez-Salas, G. Pérez-Cortéz, N. Nedev, J. Nanomater. (2019) Article ID 5287632.

[3] L. Nygaard, E. Asmussen, J.H. Høg, R.C. Maheshwari, C.H. Nielsen, I.B. Petersen, J. Rastrup-Andersen, G.O. Sørensen, J. Mol. Struct. 8 (1971) 225–233.

[4] J.-U. Grabow, H. Hartwig, N. Heineking, W. Jäger, H. Mäder, H.W. Nicolaisen, W. Stahl, J. Mol. Struct. 612 (2002) 349–356.

[5] W. Jäger, H. Mäder, Z. Naturforsch. 42a (1987) 1405–1409.

[6] W. Jäger, H. Mäder, J. Mol. Struct. 190 (1988) 295–305.

[7] E. Fliege, Z. Naturforsch. 45a (1990) 911–922.

[8] E. Fliege, H. Dreizler, M. Meyer, K. Iqbal, J. Sheridan, Z. Naturforsch. 41a (1986) 623–636.

[9] V.M. Gaware, N.S. Dighe, S.R. Pattan, H.V. Shinde, D.S. Musmade, P.A. Chavan, P. Patel, Pharm. Lett. 2 (2010) 35–40.

[10] V. Van, W. Stahl, H.V.L. Nguyen, Phys. Chem. Chem. Phys. 17 (2015) 32111–32114.

[11] V. Van, J. Bruckhuisen, W. Stahl, V. Ilyushin, H.V.L. Nguyen, J. Mol. Spectrosc. 343 (2018) 121–125.

[12] H. Hartwig, H. Dreizler, Z. Naturforsch. 51a (1996) 923–932.

[13] R. Kannengießer, M.J. Lach, W. Stahl, H.V.L. Nguyen, ChemPhysChem 16 (2015) 1906–1911.

[14] K. Eibl, R. Kannengießer, W. Stahl, H.V.L. Nguyen, I. Kleiner, Mol. Phys. 114, 3483–3489 (2016).

[15] L. Ferres, W. Stahl, I. Kleiner, H.V.L. Nguyen, J. Mol. Spectrosc. 343 (2018) 44–49.

[16] H.V.L. Nguyen, I. Kleiner, S.T. Shipman, Y. Mae, K. Hirose, S. Hatanaka, K. Kobayashi, J. Mol. Spectrosc. 299 (2014) 17–21.

[17] H.V.L. Nguyen, V. Van, W. Stahl, I. Kleiner, J. Chem. Phys. 140 (2014) 214303.

[18] M. Tudorie, I. Kleiner, M. Jahn, J.-U. Grabow, M. Goubet, O. J. Pirali, Phys. Chem. A 117 (2013) 13636−13647.

[19] M. Tudorie, I. Kleiner, J.T. Hougen, S. Melandri, L.W. Sutikdja, W. Stahl, J. Mol. Spectrosc. 269 (2011) 211−225.

[20] R. Ditchfield, W.J. Hehre, J. A. Pople, J. Chem. Phys. 54 (1971) 724−728.

[21] T.H. Dunning Jr., J. Chem. Phys. 90 (1989) 1007−1023.

[22] Gaussian 09 (Revision A.02), M.J. Frisch, G.W. Trucks, H.B. Schlegel, G.E. Scuseria, M.A. Robb, J.R. Cheeseman, G. Scalmani, V. Barone, B. Mennucci, G.A. Petersson, H. Nakatsuji, M. Caricato, X. Li, H.P. Hratchian, A.F. Izmaylov, J. Bloino, G. Zheng, J.L. Sonnenberg, M. Hada, M. Ehara, K. Toyota, R. Fukuda, J. Hasegawa, M. Ishida, T. Nakajima, Y.Honda, O. Kitao, H. Nakai, T. Vreven, J.A. Montgomery Jr., J.E. Peralta, F. Ogliaro, M. Bearpark, J.J. Heyd, E. Brothers, K.N. Kudin, V.N. Staroverov, R. Kobayashi, J. Normand, K. Raghavachari, A. Rendell, J.C. Burant, S.S. Iyengar, J. Tomasi, M. Cossi, N. Rega, J.M. Millam, M. Klene, J.E. Knox, J.B. Cross, V. Bakken, C. Adamo, J. Jaramillo, R. Gomperts, R.E. Stratmann, O. Yazyev, A.J. Austin, R. Cammi, C. Pomelli, J.W. Ochterski, R.L. Martin, K. Morokuma, V.G. Zakrzewski, G.A. Voth, P. Salvador, J.J. Dannenberg, S. Dapprich, A.D. Daniels, O. Farkas, J.B. Foresman, J.V. Ortiz, J. Cioslowski, D.J. Fox, Gaussian, Inc., Wallingford CT, 2009.

[23] R. Kannengießer, W. Stahl, H.V.L. Nguyen, W.C. Bailey, J. Mol. Spectrosc. 317 (2015) 50–53.

[24] W.C. Bailey, Chem. Phys. 252 (2000) 57–66.

[25] A. Jabri, V. Van, H.V.L. Nguyen, W. Stahl, I. Kleiner, ChemPhysChem 17 (2016) 2660–2665.

[26] V. Van, W. Stahl, H.V.L. Nguyen, ChemPhysChem 17 (2016) 3223–3228.

[27] R. Kannengießer, S. Klahm, H.V.L. Nguyen, A. Lüchow, W. Stahl, J. Chem. Phys. 141 (2014) 204308.

[28] Y. Zhao, D.G. Truhlar, Theor. Chem. Acc. 120 (2008) 215–241.

[29] H.B. Schlegel, J. Comput. Chem. 3 (1982) 214–218.

[30] R.D. Suenram, G.Y. Golubiatnikov, I.I. Leonov, J.T. Hougen, J. Ortigoso, I. Kleiner, G.T. Fraser, J. Mol. Spectrosc. 208 (2001) 188–193.

[31] R. Kannengießer, W. Stahl, H.V.L. Nguyen, I. Kleiner, J. Phys. Chem. A 120 (2016) 3992–3997.

[32] N. Ohashi, J.T. Hougen, R.D. Suenram, F.J. Lovas, Y. Kawashima, M. Fujitake, J. Pykad, J. Mol. Spectrosc. 227 (2004) 28–42.

[33] E. Herbst, J.K. Messer, F.C. De Lucia, P. Helminger, J. Mol. Spectrosc. **108**, (1984) 42–57.

[34] C.H. Townes, A.L. Schawlow, Microwave Spectroscopy, McGraw–Hill, New York, 1955.

[35] W.H. Press, S.A. Teukolsky, W.T. Vetterling, B.P. Fannery, Numerical Recipes – The Art of Scientific Computing, 3rd edition, Cambridge University Press, 2007.

[36] H. Dreizler, Z. Naturforsch. 16a (1961) 1354−1367.
[37] P. R. Bunker, P. Jensen, Molecular Symmetry and Spectroscopy, 2nd ed., NRC Research Press: Ottawa, Ontario, Canada, 2006.
[38] L. Ferres, J. Cheung, W. Stahl, H.V.L. Nguyen, J. Phys. Chem. A 123 (2019) 3497−3503.
[39] L. Ferres, W. Stahl, H.V.L. Nguyen, J. Chem. Phys. 151 (2019) 104310.
[40] J.-U. Grabow, W. Stahl, H. Dreizler, Rev. Sci. Instrum. 67 (1996) 4072−4084.
[41] L. Ferres, W. Stahl, H.V.L. Nguyen, J. Chem. Phys. 148 (2018) 124304.
[42] D. Jelisavac, D.C. Cortés-Gómez, H.V.L. Nguyen, L.W. Sutikdja, W. Stahl, I. Kleiner, J. Mol. Spectrosc. 257 (2009) 111−115.
[43] H.V.L. Nguyen, H. Mouhib, W. Stahl, I. Kleiner, Mol. Phys. 108 (2010) 763−770.
[44] H.V.L. Nguyen, A. Jabri, V. Van, W. Stahl, J. Phys. Chem. A 118 (2014) 12130−12136.
[45] Y. Zhao, H.V.L. Nguyen, W. Stahl, J.T. Hougen, J. Mol. Spectrosc. 318 (2015) 91−100.
[46] M. Andresen, I. Kleiner, M. Schwell, W. Stahl, H.V.L. Nguyen, ChemPhysChem 20, 2063–2073 (2019).
[47] K. Eibl, W. Stahl, I. Kleiner, H.V.L. Nguyen, J. Chem. Phys. 149 (2018) 144306.
[48] A. Kumar, J. Sheridan, O.L. Stiefvater, Z. Naturforsch. 33a (1978) 145−152.
[49] J.B. Graneek, W.C. Bailey, M. Schnell, Phys. Chem. Chem. Phys. 20 (2018) 22210−22217.
[50] T. Nguyen, C. Dindic, W. Stahl, H.V.L. Nguyen, I. Kleiner, Mol. Phys. (2019). DOI: 10.1080/00268976.2019.1668572
[51] R. F. Daley, Organic Chemistry, Part 1 of 3, Edition 1.3, Daley Press (2013).
[52] H. D. Rudolph, K. Walzer, I. Krutzik, J. Mol. Spectrosc. 47 (1973) 314−339.
[53] L. Ferres, K.-N. Truong, W. Stahl, H.V.L. Nguyen, *ChemPhysChem* 19 (2018) 1781−1788.
[54] E.G. Schnitzler, B.L.M. Zenchyzen, W. Jäger, ApJ 805 (2015) 141.

Table of Content Image